RESEARCH ARTICLE OPEN ACCESS

Evaluating Different ALD Techniques on NCM811 Cathodes to Mitigate Degradation and Improve Cycle Life

Michael Dohrmann[1,2] | Frauke Langer[1,3] | Sören Thieme[1] | Sylvio Indris[2,4] | Helmut Ehrenberg[2]

[1]Mercedes-Benz AG, Stuttgart, Germany | [2]Karlsruhe Institute of Technology (KIT), Institute for Applied Materials - Energy Storage Systems (IAM-ESS), Eggenstein-Leopoldshafen, Germany | [3]Chemistry of Thin Film Materials (CTFM), Friedrich-Alexander University Erlangen-Nürnberg, IZNF, Erlangen, Germany | [4]Applied Chemistry and Engineering Research Centre of Excellence (ACER CoE), Université Mohammed VI Polytechnique (UM6P), Ben Guerir, Morocco

Correspondence: Sylvio Indris (sylvio.indris@kit.edu)

Received: 10 March 2026 | **Revised:** 21 May 2026 | **Accepted:** 28 May 2026

Keywords: atomic layer deposition | cathode | coating | electrochemistry | fluidized bed | materials science

ABSTRACT

We used two different techniques of atomic layer deposition (ALD) to prepare AlO_x-coated $LiNi_{0.8}Co_{0.1}Mn_{0.1}O_2$ (NCM811) materials as cathodes for Li-ion batteries. The first approach was to use a fluidized bed reactor in order to coat the NMC811 powder before electrode film preparation and calendering with the goal of obtaining a dense coating on each particle of this powder. The second approach was to coat the electrode after film preparation and calendering by spatial ALD, with the possibility to prepare gradients of the coating material. We present an in-depth structural characterization of the prepared electrodes and their electrochemical performance, and we reveal the advantages and disadvantages of both approaches.

1 | Introduction

Due to the high demand for mobile energy storage and its estimated growth in the upcoming years, the research on lithium-ion energy storage systems has accelerated substantially. The requirements for lithium-ion batteries regarding energy density, longevity, safety, and fast charging/discharging capabilities are higher than ever and will continue to increase with growing demand [1–5]. High-nickel cathode active materials (CAM) of the layered oxide structure type with the general formula $LiNi_xCo_yMn_zO_2$, where $x + y + z = 1$ and $x \geq 0.8$, commonly known as NCM811 for $x = 0.8$ and $y = z = 0.1$, are one of the most anticipated cathode materials for applications with high energy demand, such as electric vehicles [6–9]. While the energy density of those high nickel NCMs improves with rising nickel content (Ni90 > Ni80 > Ni50 > Ni33), the material suffers from faster degradation than its low nickel content analogs (e.g., NCM523, NCM111). The main cause for the faster degradation is the lower intrinsic stability of the layered oxide crystal phase [10–12]. In contrast to lower nickel NCMs, a H2-H3 phase transition occurs at voltages close to 4.3 V versus Li/Li^+ for the high nickel NCMs. The stress caused to the crystal by continuous H2-H3 transitions promotes the structural change from the electrochemically active layered phase into less active spinel-type and ultimately into the inactive rock-salt configuration. The structural changes start at the surface of the particles and are promoted by the release of highly reactive singlet oxygen from the crystal lattice, which subsequently leads to parasitic side reactions at the cathode–electrolyte interface [12–14]. Not only acidic products of such side reactions but also transition metal ions extracted from the NCM surface dissolve into the electrolyte. There, they migrate to the surface of the anode electrode and negatively impact the solid electrolyte interphase (SEI). The changes in the SEI lead to impedance growth, consumption of active lithium ions, and safety risks [14–16]. On the cathode side, analog to the SEI on the anode side, the CEI (cathode–electrolyte interphase) is formed. Although the CEI has similarities to the SEI in regard to composition, the structure of the CEI is rather thin and offers limited protection against electrolyte exposure [17].

To mitigate the oxygen release, decomposition of the electrolyte, and the dissolution of transition metals, various kinds of coatings are commonly applied to the surface of the NCM particles to act as artificial CEI. In this regard, the barrier layer must fulfill specific requirements. To effectively reduce the parasitic side reactions without limiting the overall performance of the electrode, the artificial CEI should be thin, conformal, nonreactive with the electrolyte as well as the NCM surface, and express high permeability for lithium ions.

Atomic layer deposition (ALD) has shown great potential to achieve the formation of such barrier layers with the desired properties, and a variety of materials, such as Al_2O_3, TiO_2, or ZrO_2, were investigated [18–21]. While there is a selection of publications focusing on coating and substrate materials, limited attention was devoted to the different techniques for the application of ALD coatings. Two variants can be highlighted based on their potential for upscaling and industrial application. Fluidized bed reactor ALD (FBR-ALD) applies the coating on the NCM powder before processing to an electrode film [22–24]. In contrast, coating of the accessible surface of the final-processed composite cathode film is at the focus of spatial ALD (S-ALD) [25].

In this paper, we compare and evaluate both ALD techniques based on their technical applicability as well as their effects on the physicochemical and electrochemical properties of the manufactured cathode electrodes using various analytical and electrochemical methods. For the first time, GD-OES has been employed to determine the coating material distribution throughout the electrode. Due to its high sensitivity and applicability for depth profiling, it has proven to be a useful tool for investigating the content and distribution of elements in porous electrodes [26].

2 | Materials and Methods

2.1 | FBR-ALD on NCM Powder

As-synthesized, washed polycrystalline NCM811 was kindly provided by an established CAM supplier as an intermediary stage material. For commercial use, a protective particle coating is commonly applied for NCM811-type CAMs. In our case, the NCM was washed after synthesis to remove residual surface contaminants, but was not further processed (no surface coating).

The company Powall performed the deposition of the aluminum oxide coating on the NCM powder in a FBR. The schematic of the reactor and the process is shown in Figure 1. 150 g of NCM powder was filled in the reactor and heated to 150°C. A constant flow of 150°C preheated nitrogen carrier gas was applied to fluidize the sample. The first half cycle of the deposition was initiated by applying a 300 s pulse of evaporated trimethylaluminum (TMA) precursor at 150°C to the gas flow. In the reactor, TMA molecules are chemisorbed to the NCM particles until their surface was saturated, and the excess precursor was purged with nitrogen for 300 s. In the second half cycle, a 100 s pulse of 150°C water vapor was used to substitute the organic methyl groups of the TMA with oxygen, thus forming an aluminum oxide layer. The reactor was again purged with nitrogen for 300 s to dispose of reaction byproducts and residual water molecules. The ALD full cycle was repeated 5, 10, or 15 times to achieve level 1 (lvl 1 FBR-ALD), level 2 (lvl 2 FBR-ALD), and level 3 (lvl 3 FBR-ALD) of the coating, respectively.

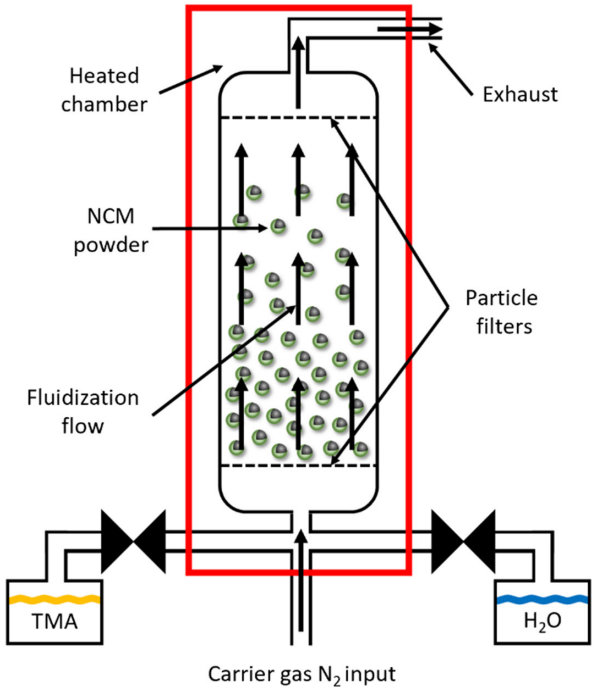

FIGURE 1 | Schematic representation of a fluidized bed ALD reactor.

2.2 | Electrode Preparation

All materials were stored and handled in an argon-filled glovebox (MBraun, UNILAB, $H_2O < 0.1$ ppm, $O_2 < 0.1$ ppm). The mixing and casting of the slurry, as well as the pre-drying, were carried out in a laboratory atmosphere (T = ca. 21°C, relative humidity = ca. 45%). All used components, except the coated NCMs, were purchased from commercial suppliers. The electrodes were fabricated by mixing 1.38 wt.% PVDF binder, 1.50 wt.% carbon black, 0.08 wt.% single-walled carbon nanotubes, and 97.04 wt.% of the bare or FBR-ALD-coated NCM in NMP (*N*-methyl-2-pyrrolidone) in a 90 ml container in a Thinky-type mixer. The solid content of the slurry was adjusted to 60 ± 1% by starting with a higher solid content (allowing better mixing of the components) and then adding solvent as needed before casting a homogenous wet film with a 200 µm gap doctor blade (BYK Instruments) on aluminum foil (20 µm thickness). The wet electrode was pre-dried on a hot plate at 100°C until the NMP was evaporated, followed by final drying under vacuum at 80°C for 12 h. The loading after drying was 15.0 ± 0.5 mg/cm^2 for all electrodes, which translates into an area capacity of 3.0 ± 0.1 mAh/cm^2 at a C/10 rate at 25°C. The dried electrodes were calendered with a lab calender (Ingecal) to a density of 2.9 ± 0.1 g/cm^3.

2.3 | Spatial ALD on Cathode Electrodes

The company SALD performed the aluminum oxide coating on calendered electrodes on DINA4-size electrode sheets. The chemical process for the application of the coating on the electrode was

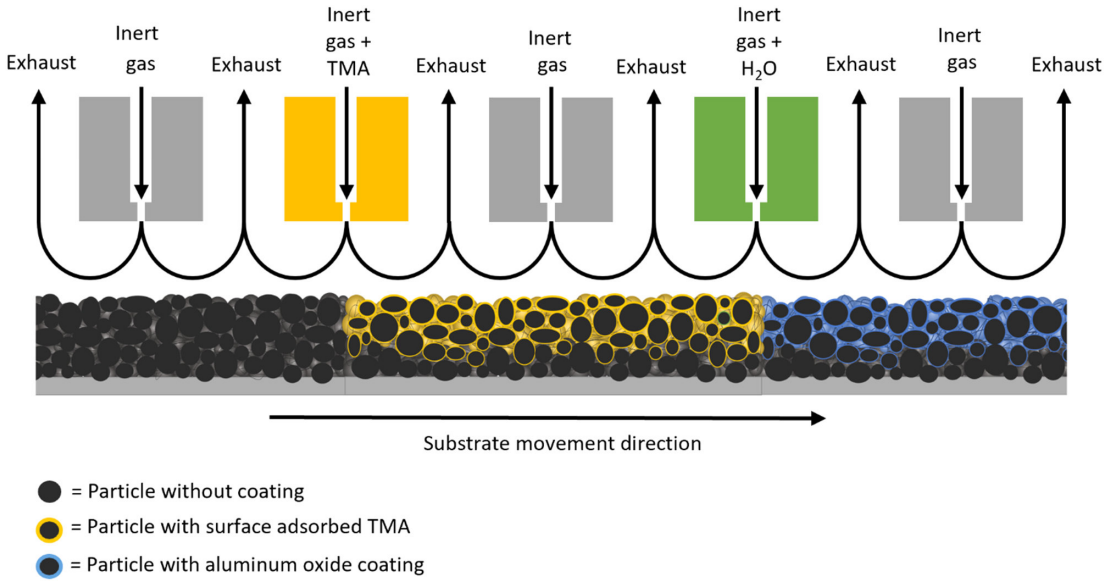

FIGURE 2 | Schematic representation of a spatial ALD reactor.

similar to the process conducted by Powall for the NCM powder coating. The process also consists of two half-cycles with the precursors TMA and water, respectively. However, the application method differed considerably, as can be seen in Figure 2. The reactor, which can be used for coating thin, porous substrates, separates the two half-cycles spatially (S-ALD) instead of chronologically (FBR-ALD). The substrate, here the calendered electrode, moves under the reactor heads that provide the different phases of the full cycle in a series of compartments. The purging and pulse time is hereby determined by the speed of the substrate under the reactor. The speed was set to 120 mm per second. The reactor temperature was adjusted to 105°C in accordance with the physical properties of the components of the electrode composite, especially the deformation temperature of the PVDF binder. The ALD full cycle was repeated 5, 10, and 15 times for level 1 (lvl 1 S-ALD), level 2 (lvl 2 S-ALD), and level 3 (lvl 3 S-ALD) of the coating, respectively.

2.4 | Surface Analysis and Imaging by XPS, TEM/EELS, and SEM

The elemental composition of the surfaces of the commercially available and intermediary stage NCMs was analyzed with a photoelectron spectrometer of the type "K-Alpha" by Thermo VG Scientific. Monochromatized Al K_α (1486.6 eV) radiation was used for the measurements.

The transmission electron microscope (TEM) imaging was performed with a Zeiss Crossbeam 550 JEOL ARM 200F with probe corrector. The additional electron energy loss spectroscopy (EELS) and energy dispersive spectroscopy (EDS) were measured with a Gatan Quantum ER EELS and a JEOL Dual EDX system, respectively. The samples were prepared by sputtering with platinum and creating a cross-section with a focused ion beam (FIB).

The scanning electron microscope (SEM) images were recorded with a JEOL JSM-7900F. An ion polisher, Hitachi IM400plus, was used to prepare the cross sections for the SEM investigation.

2.5 | Electronic Resistivity

A HIOKI RM2610 electrode resistance measurement system with an RM2611 measuring head was used to evaluate the influence of the various applied coatings on the electronic conductivity of the composite layers. The resistivity of the aluminum current collector was $2.7 \cdot 10^{-6}$ Ω·cm and its thickness was 20 µm. For the measurement, the auto range setting was used, which varied depending on the properties of the sample: 1 MΩ (10 µA) for cathodes with conductive additive, and 10 MΩ (1 µA) for cathodes without conductive additive. 15 mm diameter discs were placed under the 46-probe head for the measurement before they were used to build coin-type half-cells.

2.6 | BET Surface Analysis

The accessible surface for both the NCM powder as well as the electrode composite layer for selected samples was determined via 5-point BET physisorption measurements with krypton gas as adsorbate. The relative pressure for those measurements was between 0.12 and 0.22 p/p_0. The measurements were performed with a QuadraSorb Station 3 by Quantachrome. Before performing the physisorption measurement, the samples were dried at 80°C for 2 h under vacuum.

2.7 | Elemental Distribution via Inductively Coupled Plasma Optical Emission Spectroscopy (ICP-OES)

0.1 g of the sample was digested under pressure in a microwave Mars 6 by CEM in 10 ml of a mixture of 75 mol.% hydrochloric acid and 25 mol.% nitric acid (aqua regia) at 170°C. The solution

was then filtered, transferred quantitively, and measured with an ICP-Blue spectrometer by Spectro.

2.8 | Depth Profiling via Glow Discharge Optical Emission Spectroscopy (GD-OES)

A GDA750 spectrometer by Spectruma with an air-sealed chamber was used to perform the GD-OES measurements with argon 5.0 as discharge gas. For all measurements, radio frequency (rf) power and pulsed GD were applied with an analyzing spot size of 2.4 mm diameter. Sample preparation was done by fixing the 15 mm diameter cathode disc onto a metal plate. Calibration of GD-OES was performed by producing and measuring various NCM cathodes, consisting of different ratios of nickel, manganese, cobalt, and aluminum. All calibration samples were reference-characterized by ICP-OES. Recorded emission lines are Ni (341 nm), Mn (403 nm), Co (345 nm), and Al (396 nm).

2.9 | Electrochemical Investigations and Analysis of Volume Change

Cathode electrodes were die-cut into different formats depending on the cell type for the electrochemical procedure. The weight and thickness of the prepared electrodes were measured in a normal laboratory atmosphere using an outside micrometer (Mitutoyo, S293, precision: 0.1 µm) and a precision scale (Sartorius, precision: 0.01 mg), and final-dried over night at 80°C under vacuum. The cells were assembled using a 21 µm thick, double-sided ceramic-coated polyethylene separator in a glovebox or a dry room (dewpoint: ca. −50°C), injected with carbonate-based electrolyte consisting of 1.2 M $LiPF_6$ in EC : EMC : DMC (3.0 : 3.5 : 3.5 by vol.) with 1.5 wt.% VC, then sealed and cycled with a Basytec CTS potentiostat.

For the initial validation of the specific capacity and discharge rate performance, CR2032 coin-type half-cells were prepared from die-cut 15 mm diameter cathode discs (working electrode), 19 mm diameter separator, and 16 mm diameter lithium metal chips (counter and reference electrode), filled with 150 µl electrolyte and tested in the voltage range from 3.0 to 4.3 V versus Li/Li^+. The discharge capacities were determined at a C-rate of C/10. Subsequently, higher C-rates were tested up to 10C in discharge direction. For the half-cells, the charging current was limited to 1.0 mA/cm^2 (ca. C/3 constant current (CC) followed by a constant voltage (CV) step terminating after 2 h or when reaching 10% of CC) to prevent lithium from growing dendrites, which could penetrate the separator, causing measurement errors due to short-circuits.

For a long-time cycling, pouch-type full-cells were prepared. The cathode electrodes were die-cut into pieces with a coated area of 10 cm^2 (2.5 × 4 cm). Artificial graphite was used as a reference anode (2.7 × 4.2 cm) with an area capacity of 3.30 mAh/cm^2 to match N/P = 1.1. One-layered cell stacks were manufactured using the Z-fold method. Ultrasonic welding was used to attach a nickel-coated copper tab to the anode and an aluminum tab to the cathode sheet. The cell stacks were then sealed in a 5 × 12 cm pouch bag with one side open for electrolyte filling. After vacuum drying overnight at 80°C, the manufactured pouch cells were filled with 750 µl electrolyte and vacuum-massaged 3 times before final evacuation and sealing under vacuum.

For electrochemical testing, the cells were kept under pressure between two plastic plates. The formation of the pouch cells was carried out at room temperature with a procedure consisting of 2 times C/10, 2 times C/5, and 3 times C/3 full cycles in the voltage range from 2.8 to 4.2 V. Each charge process consisted of a CC step followed by a CV step terminating after 2 h or when reaching 10% of the CC current.

After formation, the cells were charged to a state-of-charge (SOC) of 50%, and electrochemical impedance spectroscopy (EIS) was performed. A GAMRY Reference 600 potentiostat was used to conduct a 10-point potentiostatic EIS in the range from 1 MHz to 50 mHz with an excitation voltage of 10 mV in AC mode. Subsequently, the cells were taken out of the pressure jigs, and the volume of the cells was determined according to Archimedes' principle with a scale set for density determination (Kern, YDB-03 for ABT 320 4M). The cells were weighed in air and submerged in an ethanol bath, and the volume of the cell was calculated. The pouch cells were then cycled with charge and discharge rates of 1C/1C with a C/3 full checkup cycle every 50^{th} cycle at a constant temperature of 45°C. Every 100^{th} cycle, the cells were charged to a SOC of 50% and cooled to room temperature before performing EIS measurement and cell volume determination. Afterwards, cycling at 45°C was resumed after the cells were acclimated again. After 500 full cycles, the procedure was finished. The best-performing cells from the control sample (noncoated NCM811) as well as ALD-coated NCM811 were deep-discharged to 0.0 V. The cells were opened in an argon glovebox to extract cathode electrode samples for postmortem analysis. 15 mm diameter discs were punched from the cycled cathodes and tested in CR2032 coin-type half-cells in the same manner as the pristine material for revalidation.

To evaluate reproducibility and eliminate manufacturing-related errors, 3 cells were tested for pouch-type format and 5 for coin-type format for each material. All shown data comprise data sets from at least 2 pouch-type cells and 3 coin-type cells after omitting data from defective cells.

3 | Results

3.1 | Analysis of NCM Surface via XPS, TEM/EELS, EDS

To verify that no coating was present on the intermediary NCM, XPS measurements were performed on the washed NCM and its commercially available analog prior to starting the experiments, as shown in Figure S1. After processing the noncoated NCM powder and electrodes via FBR- or S-ALD, TEM images of cross sections from the final electrodes prepared by FIB were recorded to confirm that the aluminum oxide coating was deposited homogeneously and conformally on the surfaces. To properly distinguish between the coating and the bulk NCM, as well as verify the correct configuration of the deposited aluminum oxide, EELS of oxygen was performed, and the chemical phases of the different species, as represented in Figure S2, were mapped using

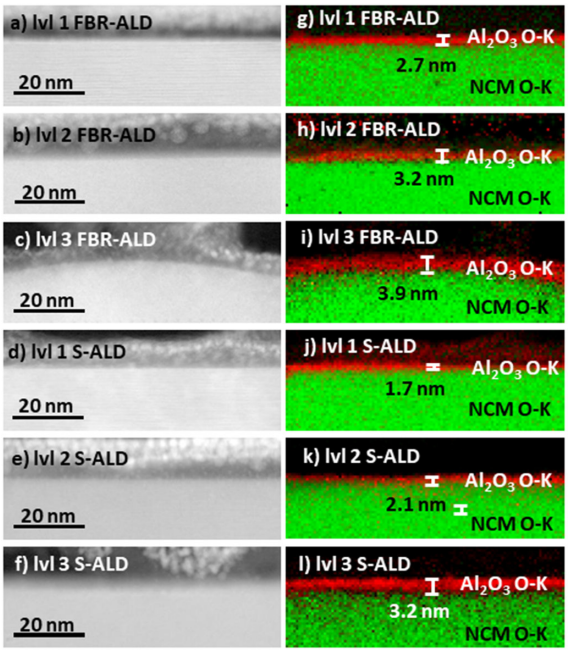

FIGURE 3 | (a–f) TEM-annular dark field (ADF) imaging of the FIB-cross section of coated NCM-particles from lvl 1-3 FBR-ALD as well as lvl 1-3 S-ALD electrodes and (g–l) chemical phase mapping of the respective ADF section calculated by MMLS fitting of the EELS data.

multi linear least square (MMLS) fittings. Figure 3 shows that the bulk NCM and the applied aluminum oxide coatings are clearly distinguishable by comparing the chemical states of the different oxygen species. All investigated coatings appear smooth and conformal in the area probed via TEM/EELS. Thus, we assume that island-growth of alumina particles was avoided in the ALD processes. Estimates of the thickness of the coatings were derived by analysis of the extension of the mapped oxygen species assigned to aluminum oxide in the EELS mappings. The thickness of the coatings increases in a linear fashion with increasing ALD cycles, as depicted in Figure S3. The thickness ranges from 2.7 nm for lvl 1, 3.2 nm for lvl 2, and 3.9 nm for lvl 3 FBR-ALD. The S-ALD coatings show a lower growth rate starting at 1.7 nm for lvl 1, 2.1 nm for lvl 2, and 3.2 nm for lvl 3. However, the estimations using this method are highly susceptible to errors due to the nature of the sample preparation. During FIB cutting, the orientation of the lamella determines the angle of the cut relative to the coating. If the cut is not precisely orthogonal to the surface of the particle, the coating will appear thicker than it is. Furthermore, the surface topography of the NCM particles and the outflow of material during ablation have a negative impact on the thickness measurements. Therefore, it is likely that the real coating thickness is somewhat thinner (at the lower end of the depicted error bars) and in close proximity to the calculated value shown in Figure S3.

TEM-EDS spectra from the space between particles of the FIB-cut cathode lamellas were recorded. The ratio of most elements depends on the position from which the recording was taken. Therefore, a small variation in the ratio of the elements such as carbon, oxygen, fluorine, and the residual signals from the NCM elements like nickel, manganese, cobalt, and oxygen is unavoidable. In addition, it can be expected to find carbon and oxygen on the surface of the NCM from formed hydroxides and carbonates. The signal for gallium can be attributed to the sample preparation via FIB using a gallium ion beam, leaving residual traces of the element at the surface of the sample. The most reliable element to quantify the amount of aluminum deposited is the fluorine in the PVDF binder. Therefore, the measured contents of the elements are standardized to the fluorine signal, as shown in Figure 4. For NCM powder coated via FBR-ALD (particle coating), none of the metal oxide coating should be present in the pores formed between NCM particles in the electrode. This is proven by the measurements shown in Figure 4a–c. In contrast, traces of coating material (aluminum) were found in the pores for the S-ALD samples. This underlines that the ALD precursor infiltrated the porous composite layer of the cathode electrode to cover all accessible surfaces of NCM, binder, and conductive additives with a coating layer. In Figure 4d–f a clear correlation between the intensity of the aluminum signal (amount of aluminum oxide deposited in cathode pores) and the number of ALD cycles is visible. For the S-ALD samples, the ratio of the aluminum compared to the standardized fluorine signal is 0.13 for lvl 1, 0.48 for lvl 2, and 0.99 for lvl 3.

3.2 | Study of Electronic Bulk Resistivity of Cathode Composite

The influence of the applied coatings on the electrical properties of the electrodes was investigated by measuring the bulk resistivity of those electrodes. Figure 5a shows the mean resistivity of five electrodes for each ALD technique and coating level, with their respective error bars measured with the HIOKI device. It is noticeable that the electronic resistivities for all variations range from 1.62 Ω cm (lvl 3 S-ALD) to 2.52 Ω cm (lvl 3 FBR-ALD), and most of the error bars have a significant overlap. Therefore, a clear distinction between the ALD technique used and the coating level applied is not possible.

However, the electronic resistivity of the electrodes is mainly determined by the conductive additive (1.5% carbon black and 0.08% SWCNT). For better comparability, the proportion of conductive additives was the same in all investigated electrodes. To properly analyze the influence of the ALD coatings on the electronic bulk resistivity of the cathode composite, another set of electrodes was prepared, this time omitting the carbon conductive additive. In such electrodes, consisting only of active material and binder, the transfer of electrons can occur solely through the NCM particles, including their internal and external grain boundaries and interparticle interfaces. As a result, the value for the composite bulk resistivity increased by three orders of magnitude. There is also a clear trend in the resistivity growth proportional to the thickness of the coating, as shown in Figure 5. The linear correlation holds true for both ALD methods. The reference electrode shows the lowest resistivity of 0.3 kΩ·cm. For the FBR-ALD samples the resistivities are 1.46, 2.68, and 4.65 kΩ·cm for lvl 1, lvl 2, and lvl 3, respectively. For the S-ALD samples, resistivities of 2.36 kΩ·cm (lvl 1), 3.33 kΩ·cm (lvl 2), and 4.23 kΩ·cm (lvl 3) were measured. The range for the S-ALD is narrower compared to the FBR-ALD samples, and the error bars are more pronounced. This is most probably due to a more inhomogeneous distribution of the coating material for the S-ALD samples.

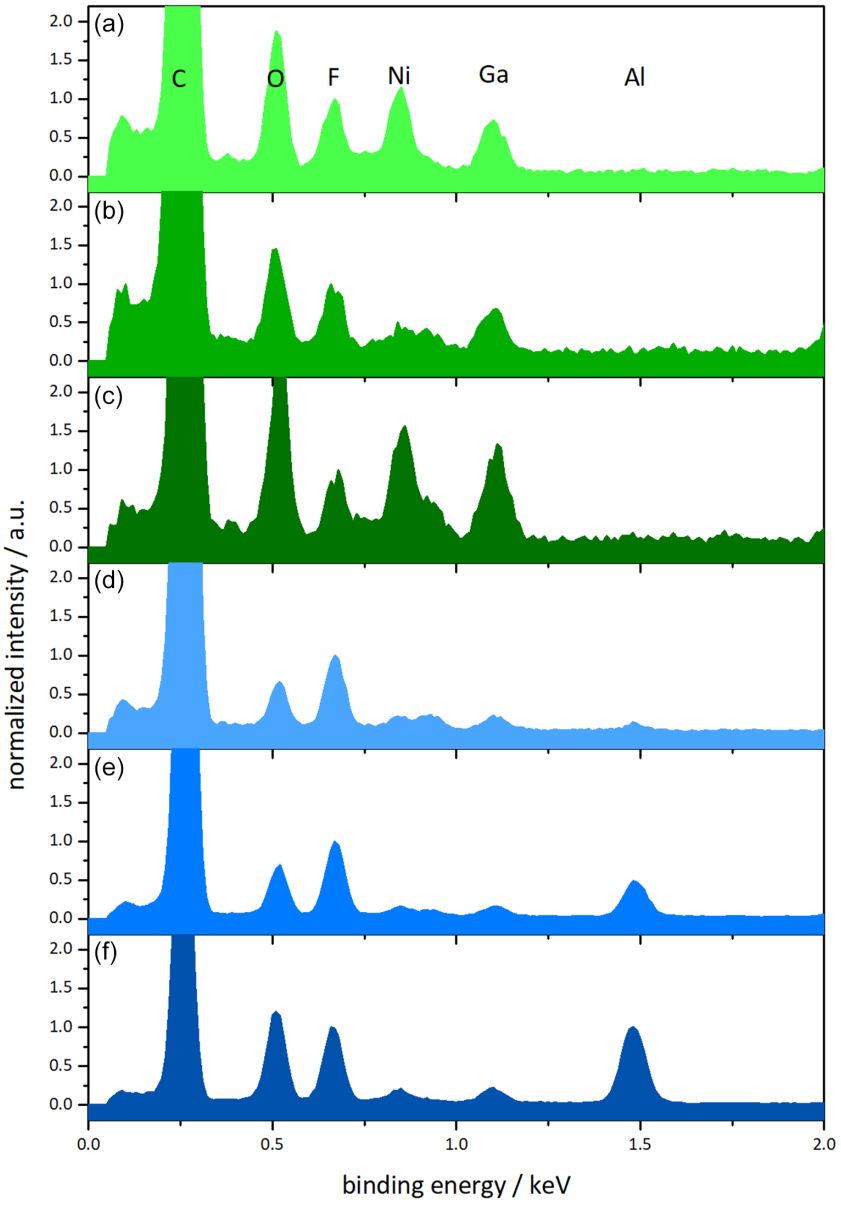

FIGURE 4 | EDS spectra measured in between particles, for (a–c) lvl 1-3 FBR-ALD and (d–f) lvl 1-3 S-ALD.

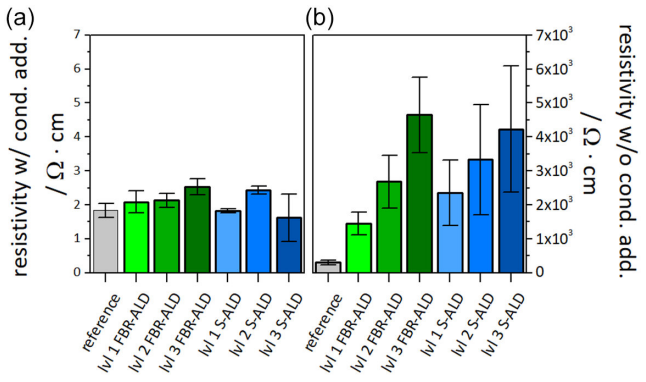

FIGURE 5 | Composite volume resistivity for cathode composites prepared (a) with and (b) without conductive additive for reference, lvl 1-3 FBR-ALD, and lvl 1-3 S-ALD samples.

3.3 | Investigation of NCM Powder and Cathode Composite Surface Area

Based on Kr-BET measurements, the specific surface area of the reference NCM powder and reference electrode was determined to be 0.64 and 1.75 $m^2\ g^{-1}$, respectively. However, the electrode consists of both the composite layer (NCM + conductive additive + binder) and the substrate foil. For this reason, the average mass and surface area of the substrate foil were determined and subtracted from the measured value, leading to a total surface area of 2.49 $m^2\ g^{-1}$ for the composite layer, which is almost four times the area of the NCM powder as shown in Figure 6. The increased surface area of the composite layer compared to the NCM powder, can be attributed to the surface contributed by the binder and conductive additives. In the ALD process, a thin and uniform coating layer is deposited on all surfaces freely accessible to the precursor molecules (TMA and water). As the NCM powder is fluidized in the FBR-ALD reactor, the coating material can, in

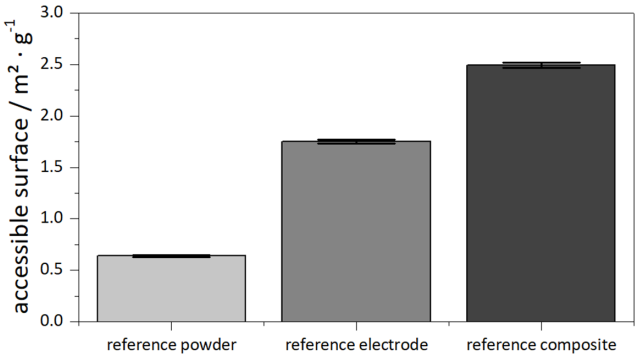

FIGURE 6 | Accessible surface areas of the reference powder and reference electrode determined by Kr-BET, as well as reference composite layer calculated by subtracting mass and surface area of the substrate foil from the reference electrode.

theory, deposit equally on the entire outer surface of the particles. In contrast, when S-ALD is applied, all accessible surfaces inside the cathode composite are covered, which includes the binder, the conductive additives, the NCM, and the substrate.

3.4 | Analysis of Deposition Rate and Local Distribution of Aluminum Oxide Coating via ICP- and GD-OES

To determine the deposition rate of the aluminum oxide in the FBR-ALD process, ICP-OES measurements of the reference material and lvl 1-3 FBR-ALD powders were performed. Figure S5 shows no aluminum in the reference material and a linear growth of aluminum content as a function of the number of full ALD cycles performed. The content of deposited aluminum ranges from 0.13 wt.% for lvl 1 FBR-ALD to 0.23 and 0.31 wt.% for lvl 2 and lvl 3, respectively.

For calibrating the results measured by GD-OES shown in Figure 7a, based on the ICP-OES results, the mean value for the aluminum content was calculated for the lvl 3 FBR-ALD sample measured by GD-OES, since the aluminum content for this sample is the highest, and the measurement is therefore less susceptible to errors. For the calculation of the mean value, the first 5 µm of the sample were disregarded because at the beginning of the measurement, material is sputtered only from the top of the electrode, where aluminum is covering the whole surface, and the bulk is only sputtered after the aluminum layer is removed. After reaching the bulk material, the aluminum content equilibrates until about 5 µm before reaching the current collector foil. Within those last 5 µm, the aluminum foil will be sputtered partially as well, resulting in a steep rise in aluminum content. This region was also disregarded for the calculation of the mean value. Compared to the aluminum content of 0.31 wt.% determined by ICP-OES, the mean value for the GD-OES measurement is significantly lower at 0.23 wt.%.

To compensate for the differences in aluminum content measured by ICP- and GD-OES and to accommodate the almost fourfold surface area of the cathode composite (S-ALD) versus NCM powder (FBR-ALD) samples, the surface density of deposited aluminum was calculated using Equation (1a), where the first term gives the aluminum ion content per surface area and the second term

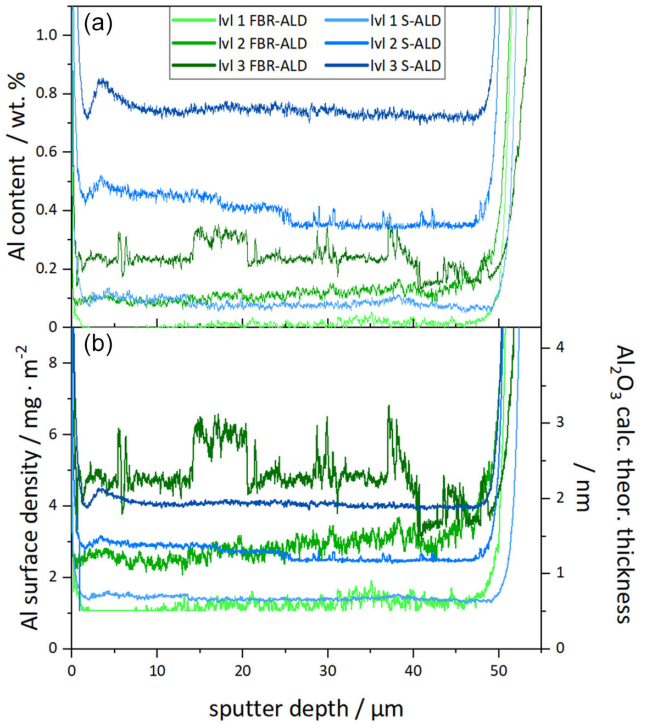

FIGURE 7 | (a) Aluminum content measured by GD-OES for lvl 1-3 FBR- and lvl 1-3 S-ALD (b) left axis: surface density of deposited aluminum; right axis: thickness of the coatings calculated from the aluminum area density and the stoichiometric composition and density of Al_2O_3.

adds the offset between ICP-OES and GD-OES measurements. The thickness of the coating was then calculated by multiplying the surface density of aluminum ions, which is shown in Figure 7b (left axis), by the stoichiometric composition and density of aluminum oxide as shown in Equation (1b). The calculated values for the coating thickness are shown in Figure 7b (right axis). For the lvl 1-3 FBR-ALD samples, coating thicknesses of 0.6, 1.4, and 2.3 nm were calculated. For the S-ALD samples, coating thicknesses of 0.7, 1.3, and 1.9 nm were calculated for lvl 1-3, respectively, as shown in Figure S2.

General assumption for the calculation for Equation (1a), the area density of aluminum, and Equation (1b), the coating thickness, depending on the aluminum area density, stoichiometric composition, and density of Al_2O_3.

$$\rho_{Al} = \left[\frac{c_{GD}}{S_m} + \frac{c_{ICP,\,FBR3} - c_{GD,\,FBR3}}{S_{m(Powder)}}\right] \tag{1a}$$

$$h_{Al_2O_3} = \rho_{Al}\left[\frac{\left[1 + \frac{\nu_{O_2} \cdot m_{O_2}}{\nu_{Al} \cdot m_{Al}}\right]}{\delta_{Al_2O_3}}\right] 10^{-9} \tag{1b}$$

ρ_{Al} = surface density of deposited aluminum ions in $\frac{g}{m^2}$

c_{GD} = content of aluminum ions in wt.% by GD-OES

$c_{ICP,\,FBR3}$ = aluminum ion content for lvl 3 FBR-ALD in wt.% = 0.31 wt.% (determined by ICP-OES)

$c_{GD,FBR3}$ = aluminum ion content for lvl 3 FBR-ALD in wt.% = 0.24 wt.% (determined by GD-OES)

S_m = specific surface area in $\frac{m^2}{g}\left(S_{m(Powder)} = 0.64\frac{m^2}{g}; S_{m(Composite)} = 2.49\frac{m^2}{g}\right)$

$h_{Al_2O_3}$ = layer thickness of Al_2O_3 -coating in nm

ν_{O_2} = stoichiometric factor of oxide ions in Al_2O_3 = 3

m_{O_2} = atomic mass of oxide ions = 15.999 u

ν_{Al} = stoichiometric factor of aluminum ions in Al_2O_3 = 2

m_{Al} = atomic mass of aluminum ions = 26.981 u

$\delta_{Al_2O_3}$ = density of Al_2O_3 = 3.95 $\frac{g}{cm^3}$

Since the values for the calculated thicknesses are significantly lower than those derived from the TEM images shown in Figure 3, we speculate that the deposited aluminum oxide might exist, at least in part, in an amorphous state, leading to a discrepancy in density versus the crystalline aluminum oxide. As the density of amorphous aluminum oxide is lower, the calculated coating thickness would increase and result in a better agreement with the TEM results.

Furthermore, content gradients, and therefore variation in coating thickness, along the depth profile of the electrode were observed for the S-ALD coated electrodes. During the development of the S-ALD procedure, more pronounced gradients from the surface toward the substrate were observed for faster deposition rates, as shown in Figure S6. By adjusting the process speed, the homogeneity of the coating was significantly improved.

3.5 | Initial Validation of ALD-Coated Samples in Coin Type Half-Cells

The initial electrochemical validation of the cathode electrodes was carried out in coin-type half-cells versus lithium metal anodes. To evaluate the influence of the ALD coating on the NCM performance, the specific capacity was analyzed after subtracting the mass of the coating material from the NCM. For the FBR-ALD samples, the maximum contribution of the coating is 0.6 wt.% for the lvl 3 sample (0.2 wt.% for lvl 1, 0.4 wt.% for lvl 2), whereas for the lvl 3 S-ALD sample, the coating contribution is up to 1.6 wt.% (0.4 wt.% for lvl 1, 1.0 wt.% for lvl 2). The discharge C-rate capabilities are shown in Figure 8.

By introducing a coating, the usable capacity decreases proportionally to the thickness of the coating for both FBR- and S-ALD samples for all C-rates. Between the range of 4C–8C, however, this effect is more pronounced for the S-ALD samples. The reason is most likely the previously discussed complete coverage of all accessible surfaces for the S-ALD samples. Those include the surfaces of the conductive additives, which might impede some electron pathways. At the end of the rate test, the retained C/3 capacity even increases compared to the initial value measured at the beginning of the test, as shown in Table 1. The systematically lower usable capacity for the coated electrodes can be attributed to the higher electric resistivity at the surface of the active material, as discussed in Section 3.2. The increase in electronic resistivity leads to an overpotential during charge and discharge proportional to the thickness of the coating a shown in Figure 9.

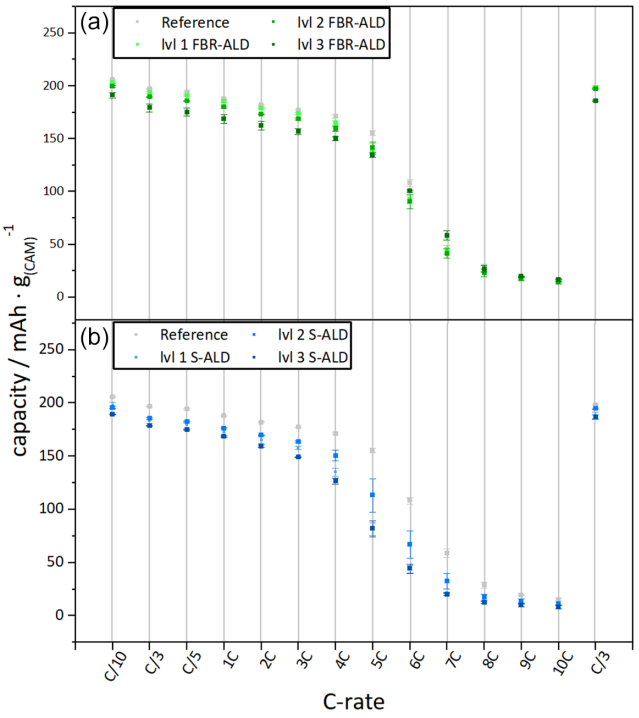

FIGURE 8 | C-rate test in coin-type half-cells for cathodes (a) lvl 1-3 FBR-ALD versus reference and (b) lvl 1-3 S-ALD versus reference.

3.6 | Analysis of Electrochemical Performance, Resistance Growth and Gassing Behavior of ALD-Coated NCM in Pouch Type Full-Cells

The cycling data for pouch-type full-cells prepared from reference, FBR-ALD, and S-ALD cathodes are shown in Figure 10. The corresponding values for the beginning of life (BOL) and end of life (EOL) capacities at C/3 rate from the check-up cycles and the calculated capacity retentions are given in Table 2. The same correlation between increasing coating thickness and decreasing initial capacity is observed, as indicated by the performance validation in coin-type half-cells in Figure 8. The degradation behavior during cycling is also influenced by the coating thickness. However, differences between cathodes prepared using the FBR-ALD and S-ALD methods are visible. The degradation behavior of lvl 2-3 FBR-ALD is similar to the uncoated reference. After stable performance up to cycle 100, the capacity loss accelerates; however, no sudden death is observed. Over 500 cycles, the samples lvl 2 FBR-ALD (75.4% retention) and lvl 3 FBR-ALD (70.3% retention) underperform the reference NCM (77.2% retention). In contrast, the lvl 1 FBR-ALD and lvl 1 S-ALD samples show a rather linear capacity degradation. Compared to the reference, the capacity loss over 500 cycles is similar at 79.9% (lvl 1 S-ALD) or lower at 83.4% (lvl 1 FBR-ALD). However, the lvl 2 S-ALD and lvl 3 S-ALD samples show a significantly more stable

TABLE 1 | C/3 discharge capacities measured in coin-type half-cells.

	Initial capacity (C/3), mAh/$g_{(CAM)}$	Retained capacity (C/3), mAh/$g_{(CAM)}$	Capacity increase, %
Reference	197.0 ± 0.4	198.27 ± 0.43	0.6
lvl 1 FBR-ALD	193.9 ± 0.9	198.72 ±0.99	2.5
lvl 2 FBR-ALD	189.3 ± 0.4	197.36 ±0.73	4.2
lvl 3 FBR-ALD	179.2 ± 3.7	186.10 ± 0.62	3.8
lvl 1 S-ALD	183.5 ± 2.9	188.17 ± 3.45	2.6
lvl 2 S-ALD	185.5 ± 0.9	194.76 ± 0.70	5.0
lvl 3 S-ALD	178.7 ± 0.3	186.95 ± 1.86	4.6

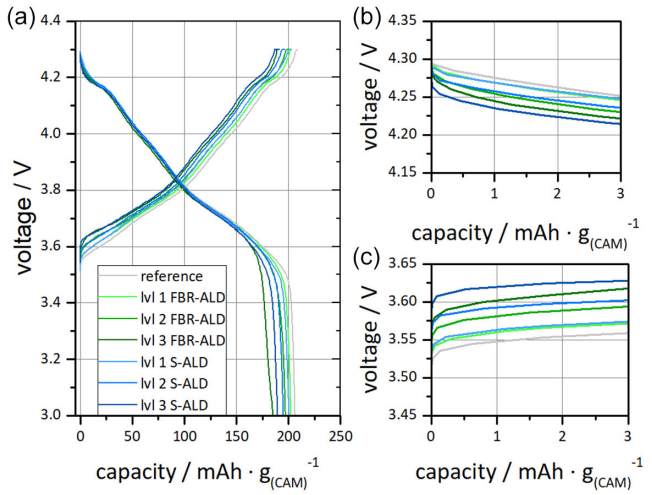

FIGURE 9 | Capacity-potential profile for one half-cell of reference, lvl 1-3 FBR-ALD and lvl 1-3 S-ALD for (a) the whole 2nd C/10 charge and discharge profiles, (b) the beginning of the discharging profiles, and (c) the beginning of the charging profiles.

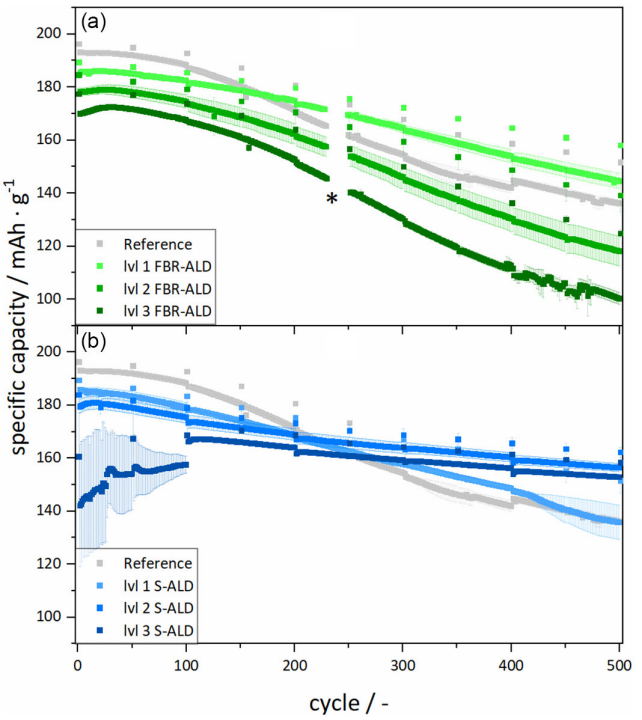

FIGURE 10 | Cycling stability test in pouch-type full-cells for (a) lvl 1-3 FBR-ALD versus reference and (b) lvl 1-3 S-ALD versus reference. The asterisk marks a gap in the recorded data caused by a downtime of the measurement system.

cycling behavior with minimal linear loss. The capacity retention in cycle 500 is as high as 88.2% (lvl 2 S-ALD) and 89.5% (lvl 3 S-ALD), considering the highest mean capacity for each sample as a reference point, except for lvl 3 S-ALD, where the initial capacity is the highest value from a single cell because the mean value is compromised by underperforming cells in the first 100 cycles (all potential-capacity profiles in Figure S7). We attribute the strong degradation behavior of the FBR-ALD samples to uncoated surfaces formed possibly due to abrasion by high shear mixing during the slurry preparation or by cracking of the polycrystalline particles in the calendaring process, as can be seen in Figure S8. For the lvl 1 S-ALD sample, accelerated capacity loss likely derives from an incomplete coating into the depth of the cathode composite layer.

The lvl 3 S-ALD sample shows an irregular behavior for the first 100 cycles. Due to the high amount of coating material deposited on the electrode surface, it is likely that some narrow entrances of the micro- and mesopores are blocked. This not only potentially increases tortuosity but also impedes electrolytes from infiltrating the pores during the wetting process. The result is an uneven electrolyte distribution. Although electronically well-connected, a certain share of NCM particles will remain inactive. After the first 100 cycles with capacity values slowly rising and stabilizing from 148.6 ± 23.7 mAh/$g_{(CAM)}$ (cycle 2, 1C) to 164.9 ± 3.2 mAh/$g_{(CAM)}$ (cycle 100, 1C), cells are taken out of the pressure jigs for gas volume determination. Before resuming the cycling experiments, the cells were massaged under pressure to homogenize electrolyte infiltration into cathode pores. The success of the approach is characterized by a sudden increase in the available capacity to 174.0 ± 0.4 mAh/$g_{(CAM)}$ (cycle 102, 1C) and stabilization at this level. The data shows that lvl 1 FBR ALD and lvl 2 S-ALD are the most promising candidates with respect to capacity utilization as well as capacity retention after 500 cycles.

To determine the reasons behind the different paces of degradation, differential capacity profiles (dQ/dV) as shown in Figure 11 were plotted for the most promising samples (for all samples in Figure S9). The reference NCM shows a drastic decline in peak

TABLE 2 | C/3 discharge capacities and gravimetric energy densities as well as state of health and energy retention after 500 cycles measured in pouch-type full cells.

	Initial capacity (C/3)	Retained capacity (C/3)	State of health (after 500 cycles)	Initial energy density (C/3)	Retained energy density (C/3)	Energy retention
	$mAh/g_{(CAM)}$	$mAh/g_{(CAM)}$	%	$Wh/kg_{(CAM)}$	$Wh/kg_{(CAM)}$	%
Reference	196.2 ± 0.9	151.6 ± 0.5	77.3	725.2 ± 3.3	541.9 ± 1.8	74.7
lvl 1 FBR-ALD	195.4 ± 0.9	163.0 ± 1.2	83.4	722.0 ± 3.3	589.4 ± 4.3	81.6
lvl 2 FBR-ALD	190.9 ± 1.5	143.9 ± 6.5	75.4	705.5 ± 5.5	508.1 ± 23.0	72.0
lvl 3 FBR-ALD	183.8 ± 0.1	129.3 ± 1.6	70.3	680.3 ± 0.4	445.7 ± 5.5	65.5
lvl 1 S-ALD	195.9 ± 0.3	156.6 ± 5.0	79.9	724.4 ± 1.1	563.0 ± 17.0	77.7
lvl 2 S-ALD	191.3 ± 2.6	168.7 ± 2.0	88.2	707.9 ± 9.6	619.6 ± 7.3	87.5
lvl 3 S-ALD	185.2 (1 cell)	165.7 ± 1.1	89.5	683.4	609.7	89.2

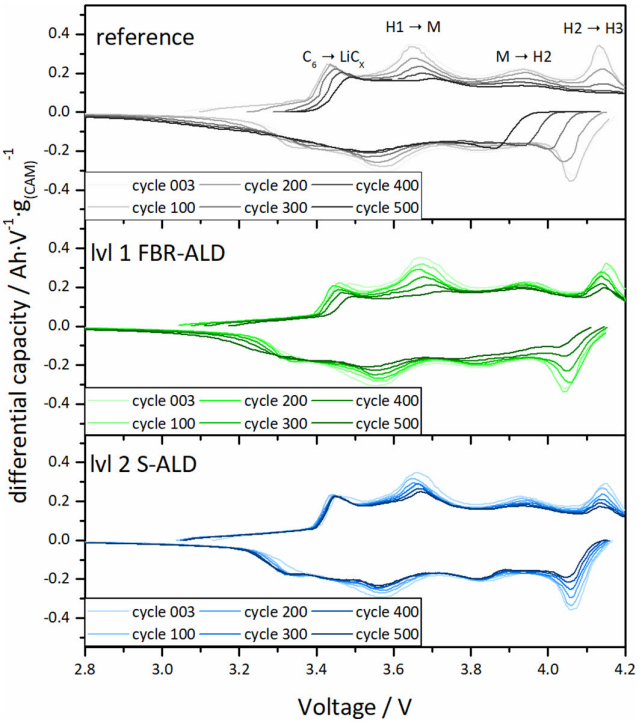

FIGURE 11 | Differential capacity profiles taken from 1C charge and 1C discharge cycles for reference NCM versus lvl 1 FBR-ALD and lvl 2 S-ALD (best-performing candidates for each ALD method).

intensity for all phase transitions as well as a large shift of the potential attributed to the H2-H3 phase transition in discharge direction from 4.06 V toward 3.86 V after 500 cycles. For the lvl 1 FBR-ALD cathode, the shift of the H2-H3 peak is strongly suppressed. However, the decline in peak intensity is still present. In addition to a successful prevention of the peak shift, the decline in peak intensity is also quite effectively mitigated for the lvl 2 S-ALD sample. The improved reversibility of the redox reactions in S-ALD > FBR-ALD > reference NCM underlines the positive effect of the applied coating layer as well as the superior quality of S-ALD versus FBR-ALD.

The correlation between coating thickness and degradation behavior for reference and coated NCM samples was further

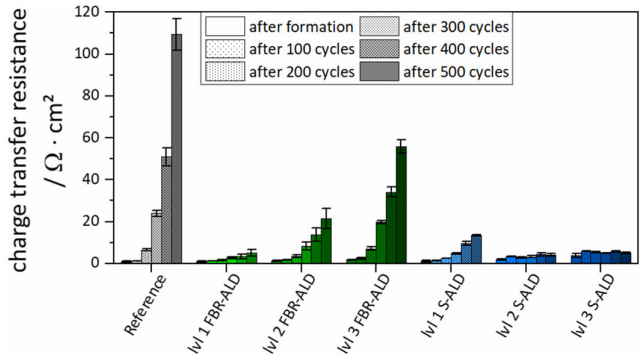

FIGURE 12 | R_{CT} values calculated from the fit with the equivalent circuit shown in Figure S10 for the reference, FBR-ALD- and S-ALD full-cells after the formation, and after every subsequent 100th cycle.

investigated by EIS measurements (Nyquist plots and equivalent circuits in Figure S10). The most conspicuous change was in the R_{CT} values, which are visualized in Figure 12. The mean R_{CT} values after the formation, after 500 cycles, and the calculated increase in percentage are given in Table 3. A strong growth of R_{CT} (+12 643%) is observed for the reference NCM due to missing protection against side reactions at the particle surface. However, NCM samples coated via the FBR-ALD method also show an increase in R_{CT}. Interestingly, this phenomenon is most pronounced for the thick lvl 3 FBR-ALD coating (+3040%) and decreases for thinner coatings (+1702% for lvl 2 FBR-ALD; +439% for lvl 2 FBR-ALD). In addition, the initial R_{CT} grows in the direction: reference < lvl 1 < lvl 2 < lvl 3, showing that particle surfaces covered by different coating thicknesses exhibit a coating-thickness-dependent initial impedance. In agreement with this finding, it is rational to assume that lithium ions preferably travel through surfaces of the lowest R_{CT}. Consequently, they will move through fresh, noncoated surface sites formed in FBR-ALD samples during processing. The thicker the coating, the higher the throughput and stress at noncoated surfaces, resulting in accelerated degradation. We see this as a rational explanation for the steep rise of R_{CT} in lvl 2 and lvl 3 FBR-ALD samples. The incomplete in-depth coating of the cathode composite for lvl 1 S-ALD results in a similar effect on R_{CT} (+1137%). The findings agree with the accelerated capacity degradation of all FBR-ALD and lvl 1 S-ALD samples. In contrast, R_{CT} is significantly more stable for fully coated lvl 2 (+121%) and lvl

TABLE 3 | R_{CT} mean values for the reference, FBR-ALD- and S-ALD full-cells after the formation and after 500 cycles.

	Initial R_{CT}, $\Omega \cdot cm^2$	R_{CT} after 500 cycles, $\Omega \cdot cm^2$	R_{CT} increase, %
Reference	0.86 ± 0.24	109.4 ± 7.5	12 643
lvl 1 FBR-ALD	0.94 ± 0.41	5.0 ± 1.5	439
lvl 2 FBR-ALD	1.19 ± 0.28	21.4 ± 4.9	1702
lvl 3 FBR-ALD	1.78 ± 0.14	55.9 ± 3.2	3040
lvl 1 S-ALD	1.08 ± 0.43	13.3 ± 0.3	1137
lvl 2 S-ALD	1.86 ± 0.31	4.1 ± 0.7	121
lvl 3 S-ALD	3.86 ± 0.95	5.0 ± 0.3	30

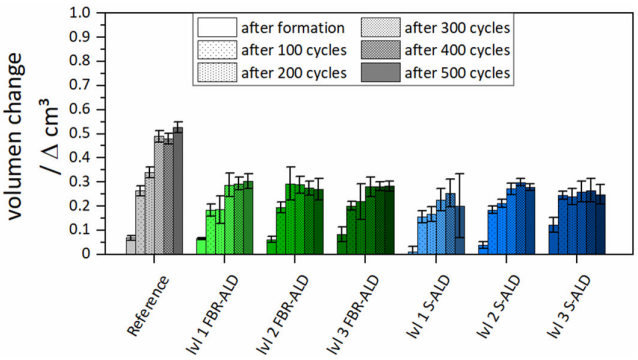

FIGURE 13 | Volume change of the pouch-type full-cells after formation and during cycling. The cells contain cathodes made from reference NCM, and FBR-ALD-coated NCM as well as S-ALD-coated NCM cathodes.

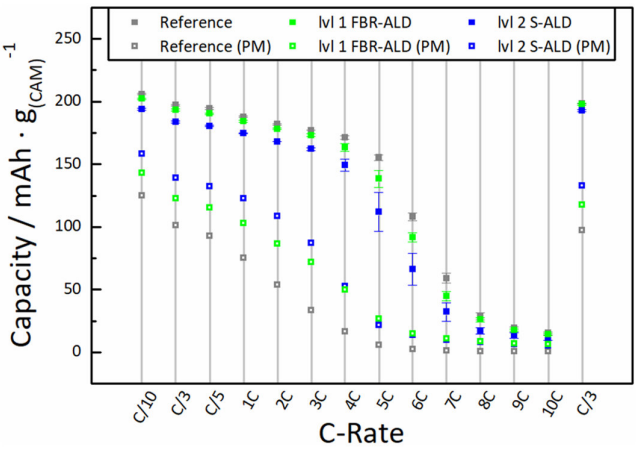

FIGURE 14 | C-rate test in coin-type half-cells for reference, lvl 1- FBR-ALD, lvl 2 S-ALD at BOL as well as EOL, each after recovering from tested pouch-type full-cells. The test conditions are the same as for the initial validation in coin-type half-cells.

3 S-ALD (+30%) samples, which translates into slow capacity loss. For lvl 3 S-ALD, the increase is formally lower, although the R_{CT} is higher than the value for lvl 2 S-ALD. This can be explained by the significantly higher initial R_{CT}, due to previously discussed anomalies with the initial performance of lvl 3 S-ALD samples.

Apart from the expansion of the active materials, the formation of gaseous decomposition products is a main contributor to the increase in cell volume during cycling. Since active materials, electrode parameters, and SOC for the investigated cells are constant throughout our study, the material expansion can be neglected. As can be seen from Figure 13, the volume of cells made from reference NCM increased by 0.53 cm^3 over 500 cycles. This is a significantly higher gas evolution compared to cells from FBR-ALD coated NCMs (0.27 to 0.30 cm^3) or S-ALD modified NCM cathodes (0.25 to 0.28 cm^3). The reduced volume change shows that applying a coating to the surface of NCM particles or cathodes via ALD successfully mitigates gas-forming side reactions. The slightly higher gas evolution for FBR-ALD samples might be attributed to direct contact between the NCM surface and electrolyte caused by defective coatings on cracked particles, as previously discussed.

For the reference material as well as lvl 1 FBR-ALD and lvl 2 S-ALD (superior samples), the electrodes from the full-cell cycling test were recovered at EOL for postmortem (PM) analysis. Figure 14 shows the retested rate performance of these EOL cathodes in coin-type half-cells. The measurement reveals a capacity loss correlating to the full-cell degradation observed previously. The reference_PM cathode still offers an extractable capacity of 101.1 $mAh/g_{(CAM)}$ at a C-rate of C/3, whereas 123.0 $mAh/g_{(CAM)}$ and 140.5 $mAh/g_{(CAM)}$ are measured for lvl 1 FBR-ALD_PM and lvl 2 S-ALD_PM, respectively. This is equal to 21.7% (FBR-ALD) and 38.9% (S-ALD) increased capacity retention.

The discharge C-rate performance of EOL cathodes is significantly worse compared to BOL, with a stronger decline already visible at low rates from C/10 to 4C. This behavior is most pronounced for the reference cathode with a low capacity retention of 33.3 $mAh/g_{(CAM)}$ at 3C. The FBR-ALD and S-ALD cathodes have capacity retentions of 71.8 and 88.19 $mAh/g_{(CAM)}$ at 3C, respectively. This correlates to a 32.9% retention for the reference_PM, 58.4% for lvl 1 FBR-ALD_PM, and 62.7% for lvl 2 S-ALD_PM. Since capacity lost in full-cells was not recoverable by the fresh source of lithium applied in half-cells, we must conclude that degradation of the full-cells was mainly driven by cathode failure.

4 | Conclusion

In this work, the effect of aluminum oxide coatings on NCM particles or cathode electrode films and its impact on the performance

of the resulting battery cell was investigated under consideration of the ALD technique used and variation of the coating thickness. The NCM powders and resulting electrodes were characterized in terms of physical properties as well as electrochemical performance.

FBR-ALD-technique was used to apply aluminum oxide coatings directly on the NCM particles before processing the NCM into electrodes. In contrast, the spatial (S-)ALD technique was used to apply coatings on previously produced electrode films.

Both techniques yielded uniform coatings in adjustable thicknesses of the desired aluminum oxide on the surface of the respective substrate, i.e., for FBR-ALD, the NCM powder before processing, and for S-ALD on the surface of the prepared electrode, with electrical properties dependent on the coating thickness as confirmed by TEM/EELS, EDS, and electrical resistivity measurements, as well as ICP- and GD-OES measurements to control deposition rate and depth profiling.

The electrochemical results are mostly in accordance with expectations based on the physical and electrical properties of the produced electrodes. For both techniques, the main influence on the performance of the resulting cells is the thickness of the coating and if there is a coating at all, as confirmed by C-rate test in coin-type half-cells and cycling and gassing behavior in pouch-type full-cells. However, clear differences in the performance dependent on the ALD technique used were observable, especially for the cycling stability, change in redox behavior shown in dQ/dV plots, and impedance growth determined by EIS measurements.

The differences in performance are most likely due to stress induced during processing of the FBR-ALD coated NCM particles, which might have damaged the coating but could not be visualized by imaging techniques due to the limited sampling size. Another factor is that the S-ALD technique applies the coating to all composite surfaces after processing to an electrode, thereby preventing damaging of the coating during processing.

On the other hand, applying the coating with SALD is more complex than with FBR-ALD since other parameters, such as porosity and pore size in the electrode, have an impact on the coating behavior, which can partly be compensated by adjusting coating parameters. With S-ALD, there is a limit to the thickness of the coating before blocking pores and impeding electrolyte distribution, and therefore decreasing performance. All coated samples show a suppression of pouch cell volume increase due to gassing during cycling.

In conclusion, it can be said that both techniques have their merits depending on the application. In our case, however, the S-ALD approach yielded higher performance enhancement.

Acknowledgments

The authors thank the ALD service providers Powall and SALD for fruitful cooperation and provision of supporting information regarding the ALD procedures. Special thanks go to Mercedes-Benz AG for funding this research.

Open Access funding enabled and organized by Projekt DEAL.

Funding

This study was supported by Mercedes-Benz AG.

Conflicts of Interest

The authors declare no conflicts of interest.

References

1. A. A. Tidblad, K. Edström, G. Hernández, et al., "Future Material Developments for Electric Vehicle Battery Cells Answering Growing Demands from an End-User Perspective," *Energies* 14, no. 14 (2021): 4223.

2. X. Han, L. Lu, Y. Zheng, et al., "A Review on the Key Issues of the Lithium Ion Battery Degradation among the Whole Life Cycle," *eTransportation* 1 (2019): 100005.

3. J. Zhao and A. F. Burke, "Electric Vehicle Batteries: Status and Perspectives of Data-Driven Diagnosis and Prognosis," *Batteries* 8, no. 10 (2022): 142.

4. X. Sun, X. Luo, Z. Zhang, F. Meng, and J. Yang, "Life Cycle Assessment of Lithium Nickel Cobalt Manganese Oxide (NCM) Batteries for Electric Passenger Vehicles," *Journal of Cleaner Production* 273 (2020): 123006.

5. A. Bills, S. Sripad, W. L. Fredericks, M. Singh, and V. Viswanathan, "Performance Metrics Required of Next-Generation Batteries to Electrify Commercial Aircraft," *ACS Energy Letters* 5, no. 2 (2020): 663–668.

6. A. Konarov, S.-T. Myung, and Y.-K. Sun, "Cathode Materials for Future Electric Vehicles and Energy Storage Systems," *ACS Energy Letters* 2, no. 3 (2017): 703–708.

7. J. Deng, C. Bae, A. Denlinger, and T. Miller, "Electric Vehicles Batteries: Requirements and Challenges," *Joule* 4, no. 3 (2020): 511–515.

8. J.-H. Kim, K.-J. Park, S. J. Kim, C. S. Yoon, and Y.-K. Sun, "A Method of Increasing the Energy Density of Layered Ni-Rich $Li[Ni_{1-2x}Co_xMn_x]O_2$ Cathodes (x = 0.05, 0.1, 0.2)," *Journal of Materials Chemistry A* 7, no. 6 (2019): 2694–2701.

9. X. Wang, Y.-L. Ding, Y.-P. Deng, and Z. Chen, "Ni-Rich/Co-Poor Layered Cathode for Automotive Li-Ion Batteries: Promises and Challenges," *Advanced Energy Materials* 10, no. 12 (2020).

10. S.-K. Jung, H. Gwon, J. Hong, et al., "Understanding the Degradation Mechanisms of $LiNi_{0.5}Co_{0.2}Mn_{0.3}O_2$ Cathode Material in Lithium Ion Batteries," *Advanced Energy Materials* 4, no. 1 (2014).

11. S.-M. Bak, E. Hu, Y. Zhou, et al., "Structural Changes and Thermal Stability of Charged $LiNi_xMn_yCo_zO_2$ Cathode Materials Studied by Combined In Situ Time-Resolved XRD and Mass Spectroscopy," *ACS Applied Materials & Interfaces* 6, no. 24 (2014): 22594–22601.

12. T. Li, X.-Z. Yuan, L. Zhang, D. Song, K. Shi, and C. Bock, "Degradation Mechanisms and Mitigation Strategies of Nickel-Rich NMC-Based Lithium-Ion Batteries," *Electrochemical Energy Reviews* 3, no. 1 (2020): 43–80.

13. Y. Xie, H. Gao, J. Gim, A. T. Ngo, Z.-F. Ma, and Z. Chen, "Identifying Active Sites for Parasitic Reactions at the Cathode-Electrolyte Interface," *The Journal of Physical Chemistry Letters* 10, no. 3 (2019): 589–594.

14. S. K. Heiskanen, N. Laszczynski, and B. L. Lucht, "Perspective—Surface Reactions of Electrolyte with $LiNi_xCo_yMn_zO_2$ Cathodes for Lithium Ion Batteries," *Journal of the Electrochemical Society* 167, no. 10 (2020): 100519.

15. C. Zhan, T. Wu, J. Lu, and K. Amine, "Dissolution, Migration, and Deposition of Transition Metal Ions in Li-Ion Batteries Exemplified by Mn-Based Cathodes – a Critical Review," *Energy & Environmental Science* 11, no. 2 (2018): 243–257.

16. J. C. Hestenes, J. T. Sadowski, R. May, and L. E. Marbella, "Transition Metal Dissolution Mechanisms and Impacts on Electronic Conductivity

in Composite $LiNi_{0.5}Mn_{1.5}O_4$ Cathode Films," *ACS Materials Au* 3, no. 2 (2023): 88–101.

17. S. Malmgren, K. Ciosek, M. Hahlin, et al., "Comparing Anode and Cathode Electrode/Electrolyte Interface Composition and Morphology Using Soft and Hard X-Ray Photoelectron Spectroscopy," *Electrochimica Acta* 97 (2013): 23–32.

18. Y. Zhao, K. Zheng, and X. Sun, "Addressing Interfacial Issues in Liquid-Based and Solid-State Batteries by Atomic and Molecular Layer Deposition," *Joule* 2, no. 12 (2018): 2583–2604.

19. E. Ahvenniemi and M. Karppinen, "ALD/MLD Processes for Mn and Co Based Hybrid Thin Films," *Dalton Transactions* 45, no. 26 (2016): 10730–10735.

20. E. Riyanto, E. Martides, G. Pikra, et al., "A Review of Atomic Layer Deposition for High Lithium-Ion Battery Performance," *Journal of Materials Research and Technology* 15 (2021): 5466–5481.

21. H. Yu, X. He, and X. Liang, "AlF_3-Al_2O_3 ALD Thin-Film-Coated $Li_{1.2}Mn_{0.54}Co_{0.13}Ni_{0.13}O_2$ Particles for Lithium-Ion Batteries: Long-Term Protection," *ACS Applied Materials & Interfaces* 14, no. 3 (2022): 3991–4003.

22. L. F. Hakim, S. M. George, and A. W. Weimer, "Conformal Nanocoating of Zirconia Nanoparticles by Atomic Layer Deposition in a Fluidized Bed Reactor," *Nanotechnology* 16, no. 7 (2005): S375–81.

23. D. M. King, X. Liang, Y. Zhou, et al., "Atomic Layer Deposition of TiO_2 Films on Particles in a Fluidized Bed Reactor," *Powder Technology* 183, no. 3 (2008): 356–363.

24. Powall – Empowdering Progress, https://www.powall.com/, 2023.

25. SALD, Spatial ALD Innovators, https://spatialald.com/, 2023.

26. F. Langer, A. Utami, J. Kirres, E. Krämer, and J. Bachmann, "GD-OES Investigations of Lithium-Ion Battery Graphite Anodes: Impact of Plasma Parameters and Electrode Properties," *ACS Applied Materials & Interfaces* 15, no. 28 (2023): 33571–33580.

Supporting Information

Additional supporting information can be found online in the Supporting Information section.